Supplementary Information

Rational Design of One-Pot Solvent-Assisted Synthesis for Multi-Functional Sn-Substituted Superionic Li Argyrodite Solid Electrolytes

Sun Hee Choi[a], Woong-Ju Kim[a], Byeong-hyeon Lee[b], Sung-Chul Kim[b], Jin Gu Kang[c,], Dong-Wan Kim[a,]**

[a] School of Civil, Environmental and Architectural Engineering, Korea University, Seoul 02841, South Korea

[b] Advanced Analysis Center, Korea Institute of Science and Technology, Seoul 02792, South Korea

[c] Nanophotonics Research Center, Korea Institute of Science and Technology, Seoul 02792, South Korea

Corresponding Author

*E-mail: dwkim1@korea.ac.kr (D.-W. Kim)

*E-mail: lucid1@kist.re.kr (J.G. Kang)

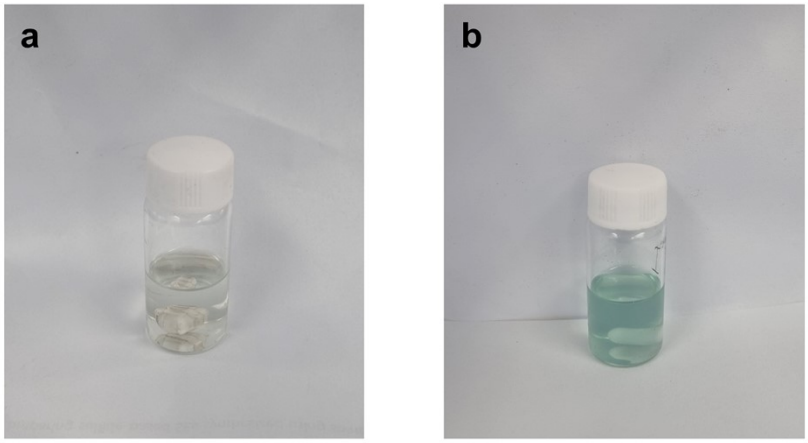

Figure S1. Photographs of acetonitrile (ACN) solutions of (a) 4% w/v LiBr and (b) 5% w/v LiI. The concentrations are the same as those used for synthesizing Li_6PS_5Br and Li_6PS_5I, respectively.

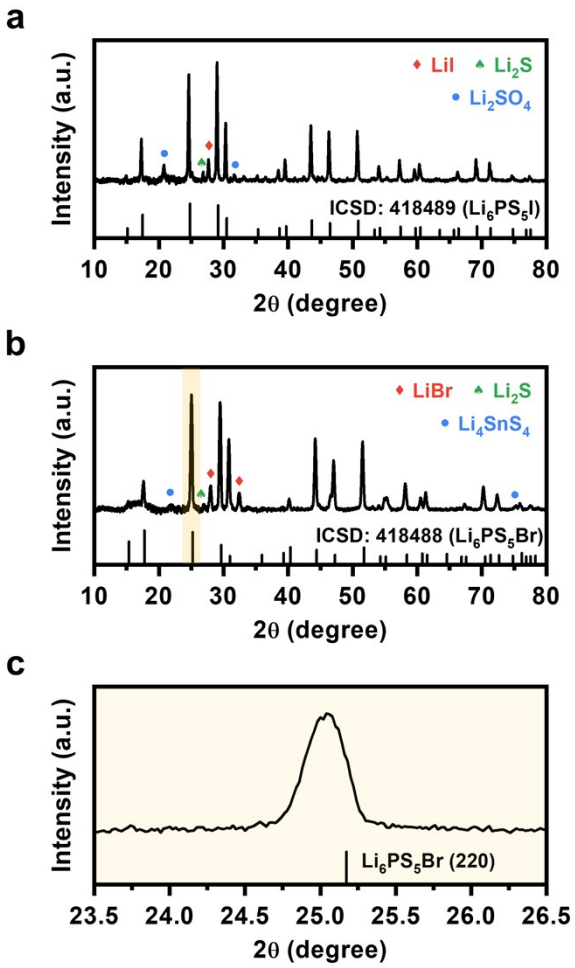

Figure S2. (a) X-ray diffraction (XRD) pattern of the sample fabricated by mixing Li_2S, LiI, and P_2S_5 simultaneously in ACN. (b) XRD pattern and (c) its magnified view in the 2θ range from 23.5 to 26.5° (shaded in yellow) for the sample prepared by simultaneously adding P_2S_5 and SnS_2 (12.5 at%) to a mixture of Li_2S and LiBr in ACN. In (c), the peak corresponding to the (220) plane exhibits a small downward shift compared to that of non-substituted Li_6PS_5Br, indicating negligible Sn substitution in the host lattice.

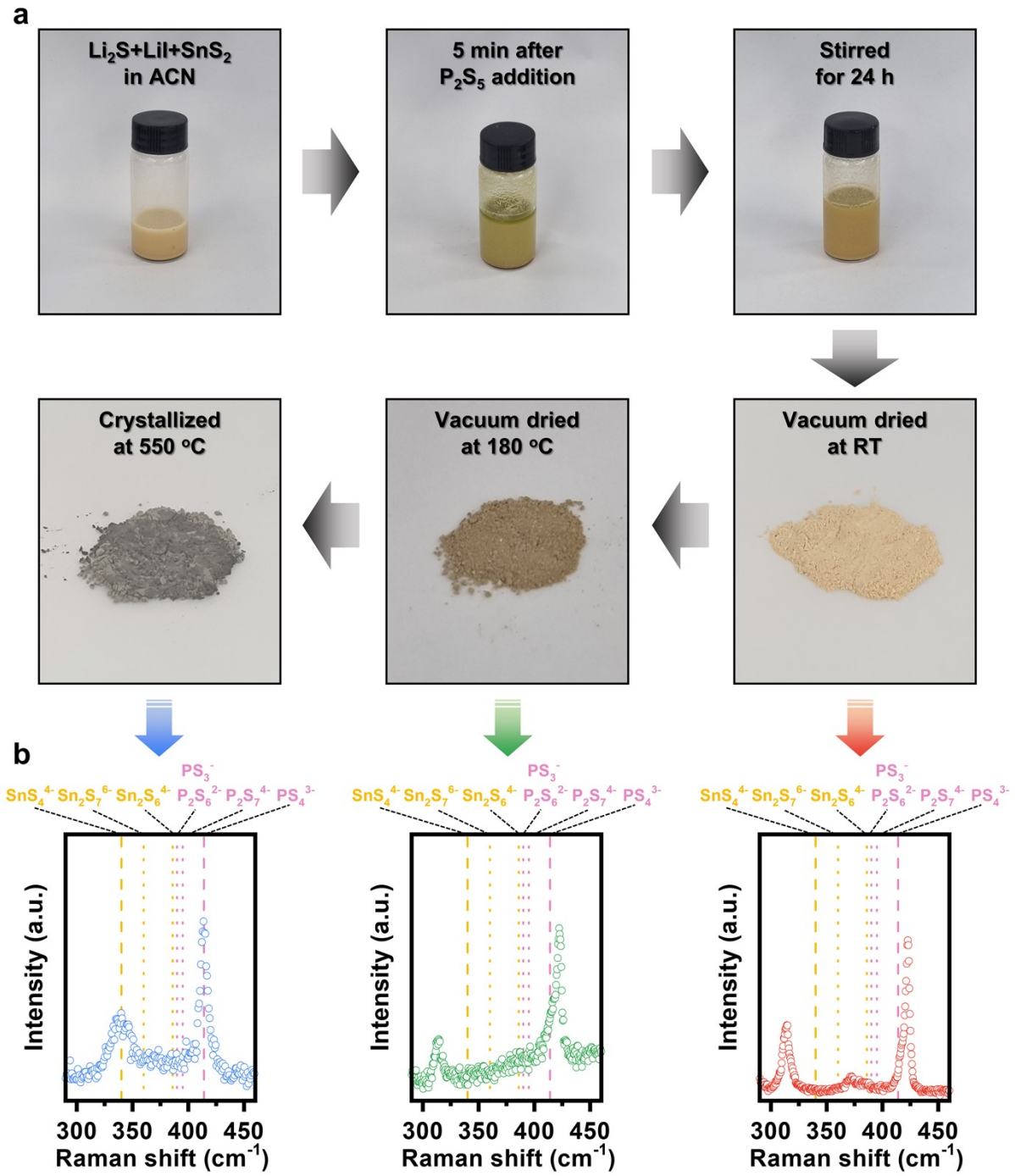

Figure S3. (a) Photographs of the ACN suspension and prepared powders taken at each fabrication step for obtaining $Li_{6.2}P_{0.8}Sn_{0.2}S_5I$. (b) Raman spectra collected after vacuum drying at ~25 °C (right panel), after vacuum drying at 180 °C (middle panel), and after heat-treatment at 550 °C (left panel). The Raman modes for various thiostannate and thiophosphate units are indicated above the plots.

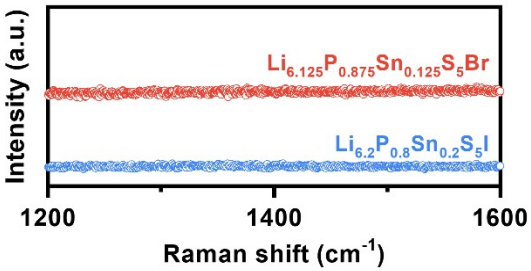

Figure S4. Raman spectra of $Li_{6.125}P_{0.875}Sn_{0.125}S_5Br$ and $Li_{6.2}P_{0.8}Sn_{0.2}S_5I$ in the range from 1200 to 1600 cm^{-1}. No D- and G-modes of carbonaceous phases are observed.

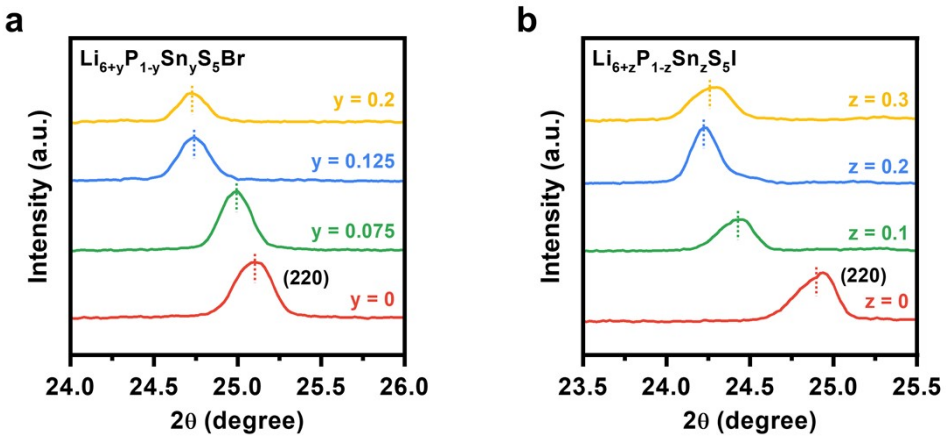

Figure S5. Magnified XRD patterns scans of (a) $Li_{6+y}P_{1-y}Sn_yS_5Br$ (y = 0, 0.075, 0.125, and 0.2) and (b) $Li_{6+z}P_{1-z}Sn_zS_5I$ (z = 0, 0.1, 0.2, and 0.3). The peak of the (220) plane shifts toward a lower 2θ value with increasing Sn substitution level. However, the peak position remains constant beyond y = 0.125 for $Li_{6+y}P_{1-y}Sn_yS_5Br$ (a) and z = 0.2 for $Li_{6+z}P_{1-z}Sn_zS_5I$ (b).

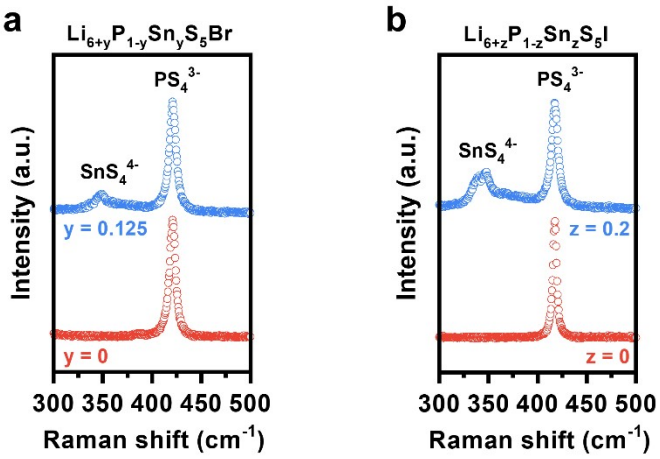

Figure S6. Raman spectra of (a) $Li_{6+y}P_{1-y}Sn_yS_5Br$ (y = 0, 0.125) and (b) $Li_{6+z}P_{1-z}Sn_zS_5I$ (z = 0, 0.2).

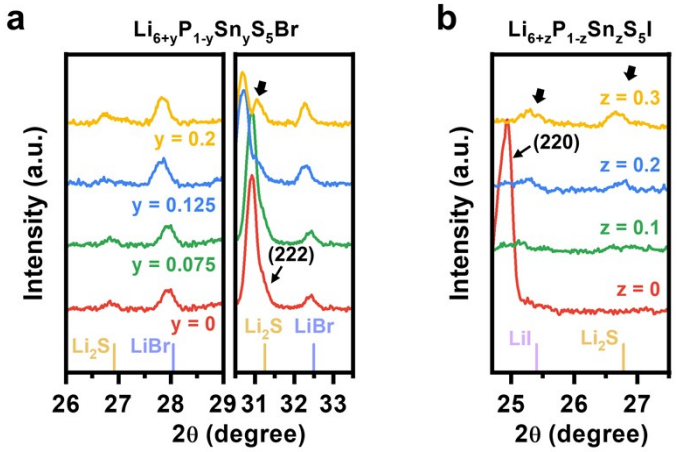

Figure S7. Magnified XRD patterns of (a) $Li_{6+y}P_{1-y}Sn_yS_5Br$ (y = 0, 0.075, 0.125, 0.2) and (b) $Li_{6+z}P_{1-z}Sn_zS_5I$ (z = 0, 0.1, 0.2, 0.3) showing the evolution of impurity phases with increasing Sn-substitution concentration. The strong peaks in each graph correspond to Li-argyrodite phases.

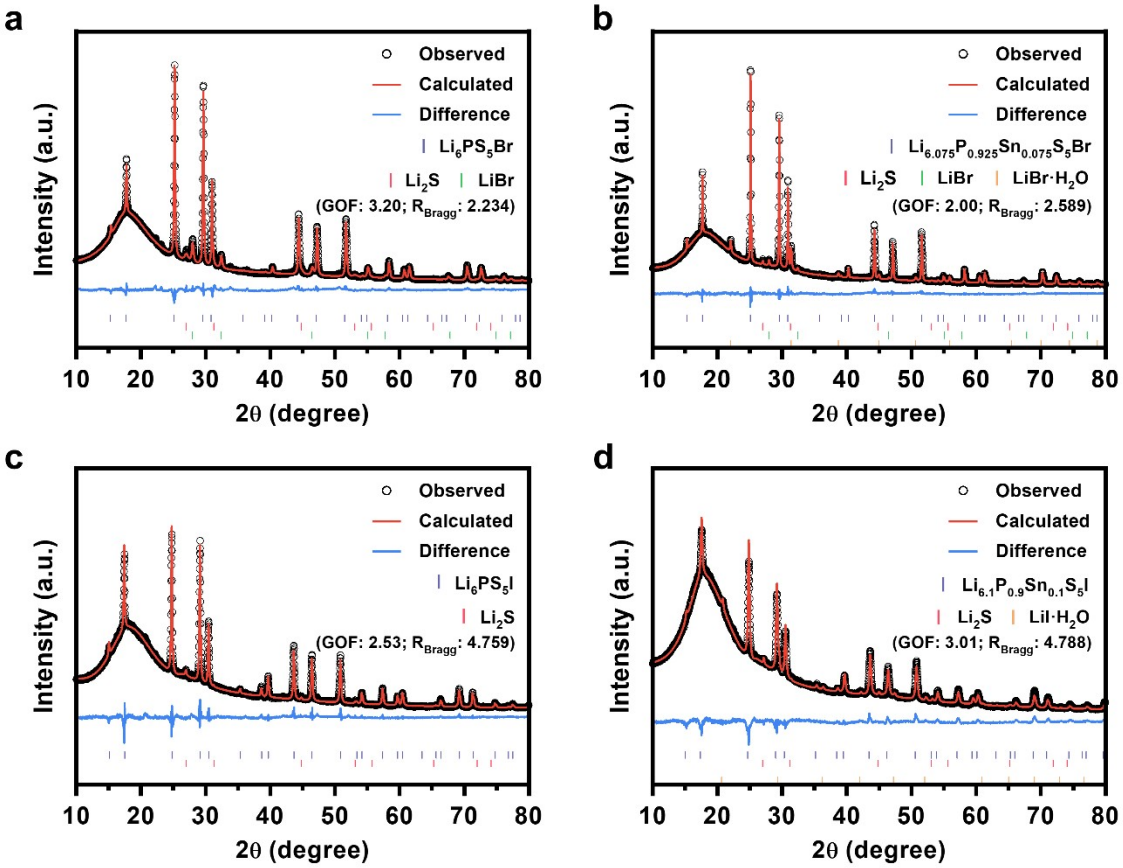

Figure S8. Low-scan speed XRD patterns and Rietveld refinement results for (a) Li_6PS_5Br, (b) $Li_{6.075}P_{0.925}Sn_{0.075}S_5Br$, (c) Li_6PS_5I, and (d) $Li_{6.1}P_{0.9}Sn_{0.1}S_5I$.

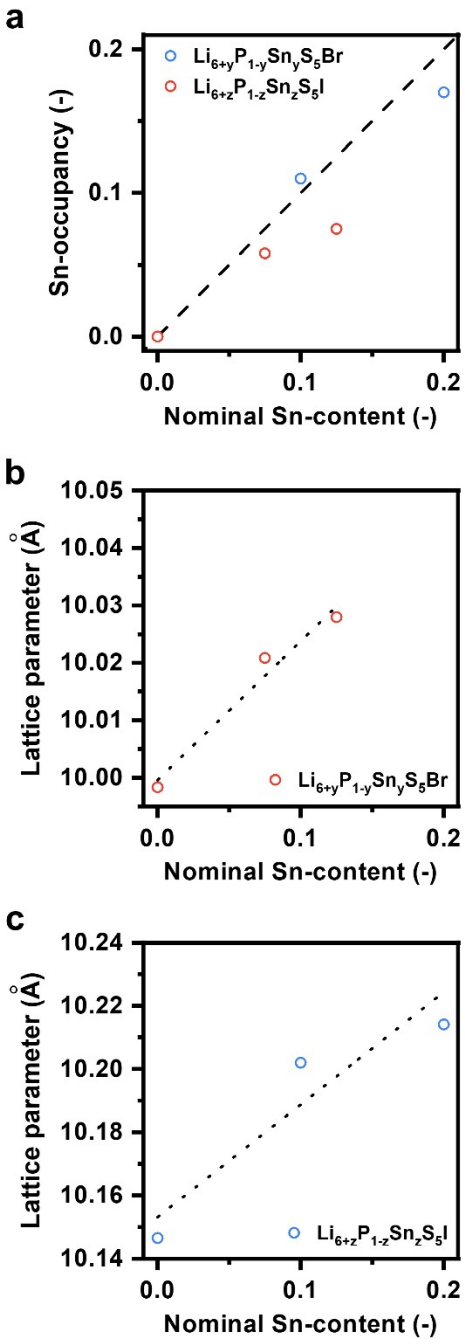

Figure S9. (a) Plot of Sn-occupancy determined by Rietveld refinement as a function of nominal Sn-content for bromide- and iodide-argyrodites. Dashed lines denotes Sn-occupancies equal to nominal Sn-content. Plots of lattice parameter determined by Rietveld refinement as a function of nominal Sn-content for (b) $Li_{6+y}P_{1-y}Sn_yS_5Br$ and (c) $Li_{6+z}P_{1-z}Sn_zSI$. The dotted lines denote fitted curves by linear regression.

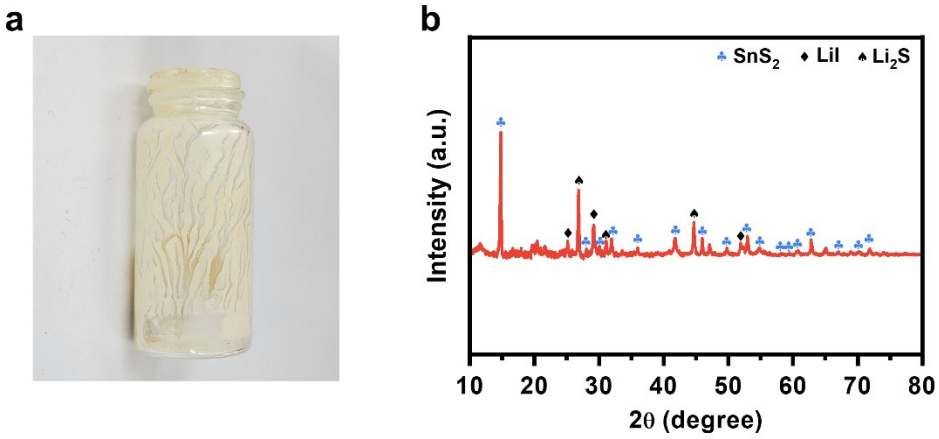

Figure S10. (a) Photograph of the unreacted sediments remained at the interior of a vial after transferring an ACN mixture suspension of Li_2S, SnS_2, LiI, and P_2S_5 to a vacuum chamber. (b) XRD pattern of the sediments.

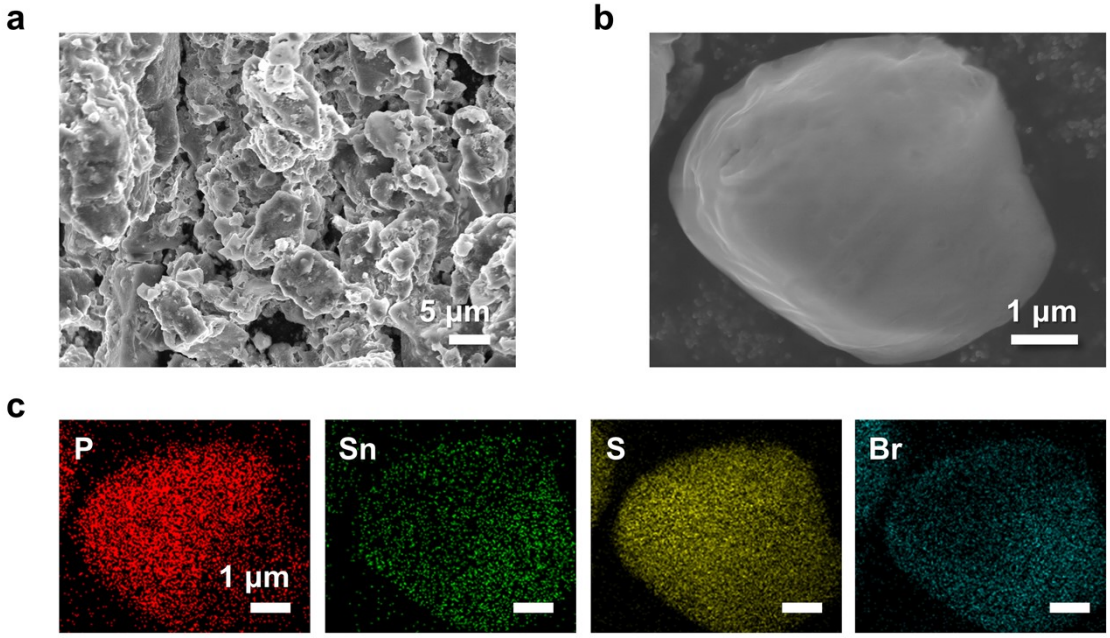

Figure S11. (a) Low- and (b) high-magnification scanning electron microscopy (SEM) images of $Li_{6.125}P_{0.875}Sn_{0.125}S_5Br$ and (c) its EDX elemental mapping results for P, Sn, S, and Br.

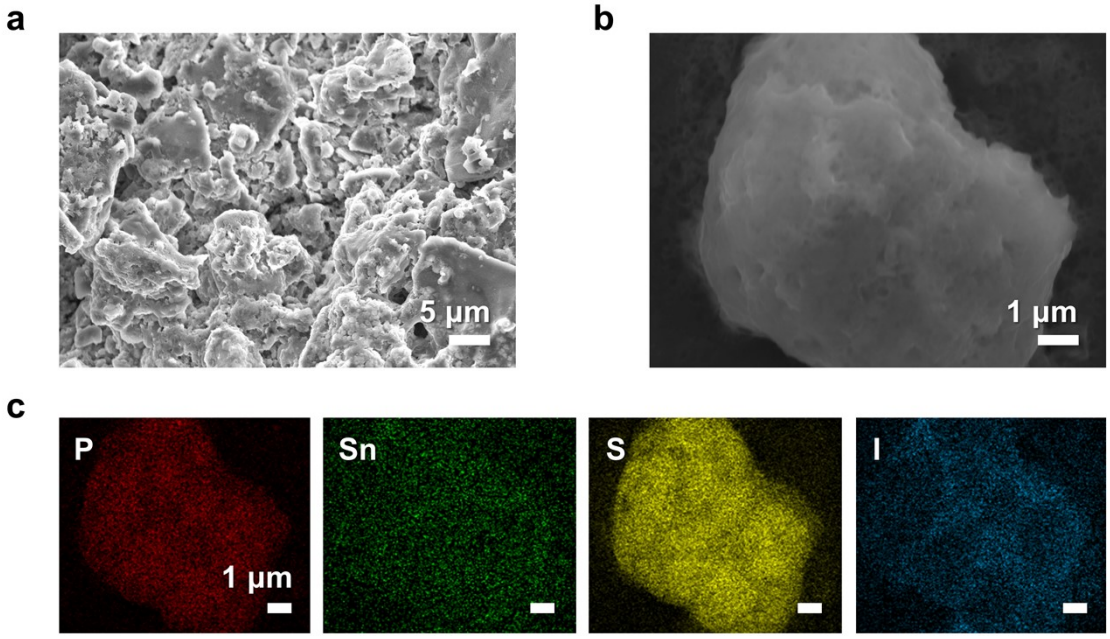

Figure S12. (a) Low- and (b) high-magnification SEM images of $Li_{6.2}P_{0.8}Sn_{0.2}S_5I$, and (c) its EDX elemental mapping results for P, Sn, S, and I.

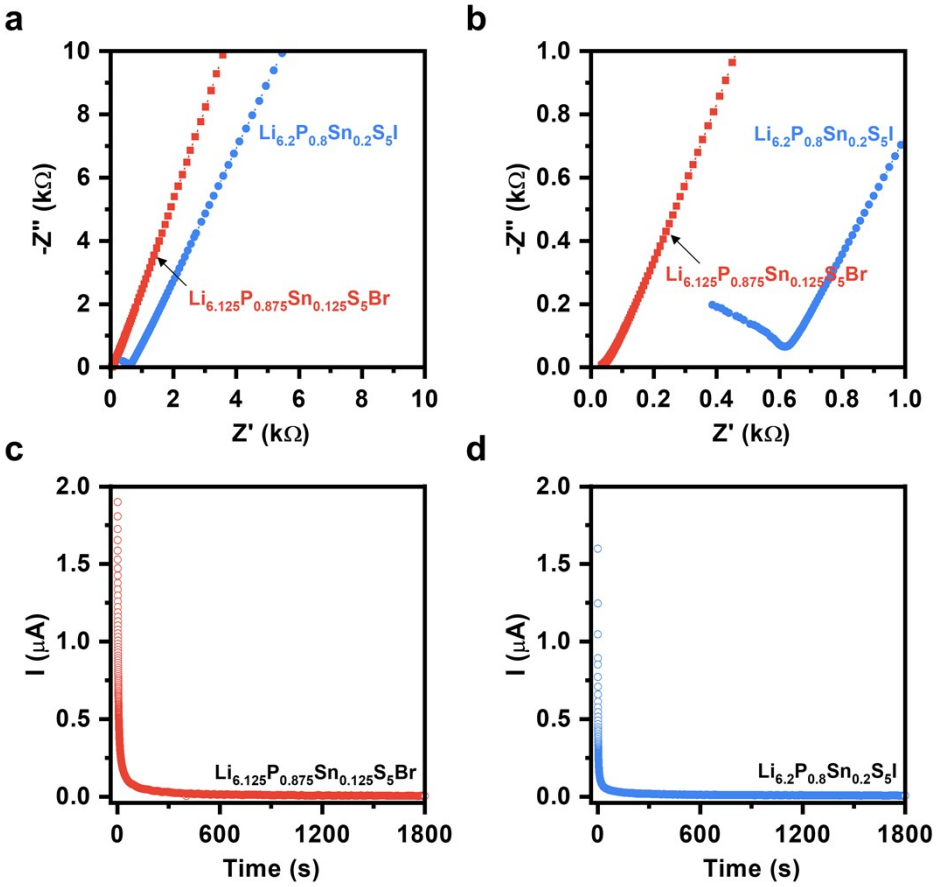

Figure S13. (a) Nyquist plots and (b) their magnified versions of $Li_{6.125}P_{0.875}Sn_{0.125}S_5Br$ and $Li_{6.2}P_{0.8}Sn_{0.2}S_5I$. DC polarization curves of (c) $Li_{6.125}P_{0.875}Sn_{0.125}S_5Br$ and (d) $Li_{6.2}P_{0.8}Sn_{0.2}S_5I$. Measurements were carried out using symmetric cells comprising solid electrolytes sandwiched between two identical Li-ion-blocking Ti electrodes.

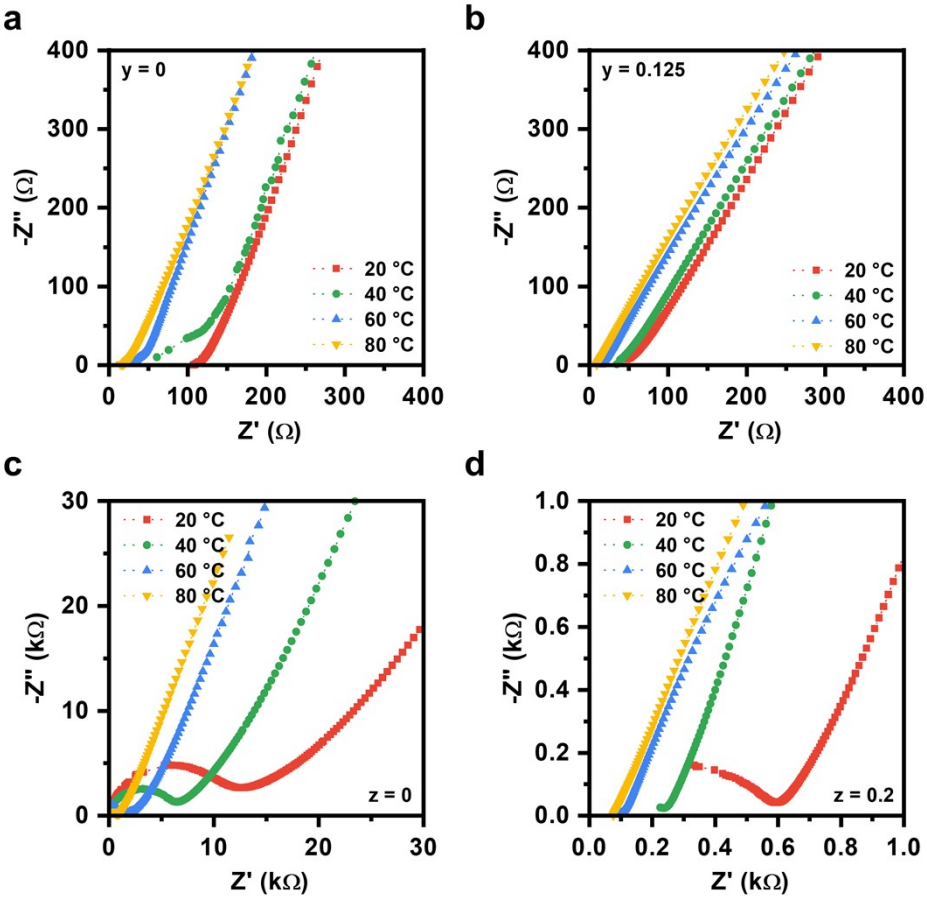

Figure S14. Nyquist plots acquired in the temperature range of 20 - 80 °C for (a) Li_6PS_5Br, (b) $Li_{6.125}P_{0.875}Sn_{0.125}S_5Br$, (c) Li_6PS_5I, and (d) $Li_{6.2}P_{0.8}Sn_{0.2}S_5I$. Measurements were carried out using symmetric cells comprising solid electrolytes sandwiched between two identical Li-ion-blocking Ti electrodes.

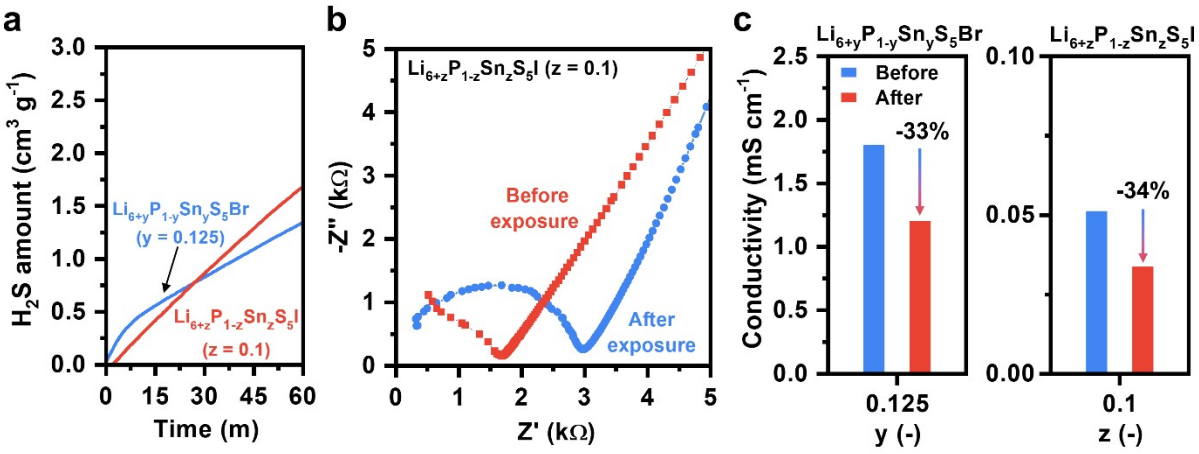

Figure S15. (a) Time-lapse detection of the amount of H_2S produced from two solid electrolytes upon exposure to air: $Li_{6.125}P_{0.875}Sn_{0.125}S_5Br$ and $Li_{6.1}P_{0.9}Sn_{0.1}S_5I$. (b) Nyquist plots of $Li_{6.1}P_{0.9}Sn_{0.1}S_5I$ before and after exposure. (c) Bar diagrams representing the changes in the ionic conductivities of $Li_{6.125}P_{0.875}Sn_{0.125}S_5Br$ and $Li_{6.1}P_{0.9}Sn_{0.1}S_5I$ after exposure.

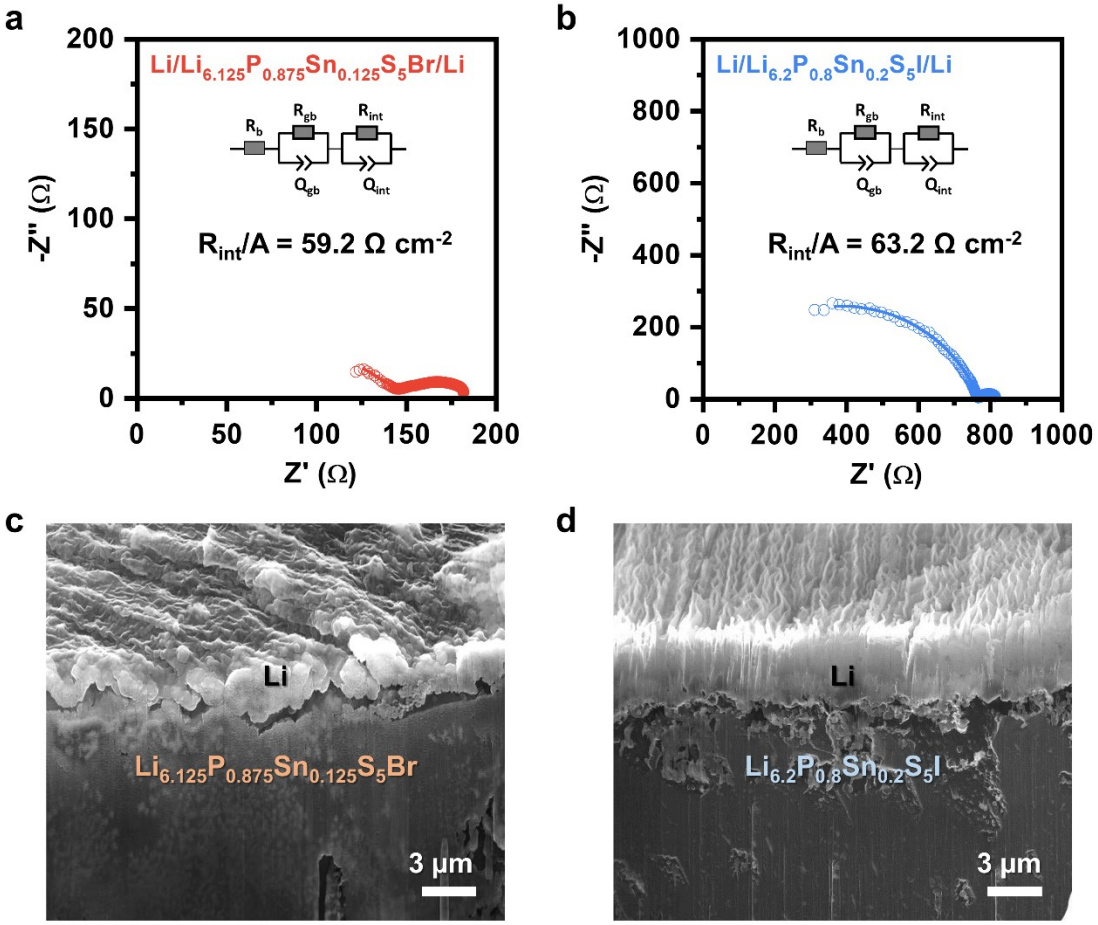

Figure S16. (a,b) Nyquist plots and (c,d) FIB-milled cross-sectional SEM images of two symmetric cells comprising two identical Li foils apart by $Li_{6.125}P_{0.875}Sn_{0.125}S_5Br$ (a,c) and $Li_{6.2}P_{0.8}Sn_{0.2}S_5I$ (b,d) after five cycles of Li deposition/stripping at 0.1 mA cm^{-2}. Insets in (a) and (b) are the equivalent circuits used for fitting the spectra. The areal interfacial resistances (R_{int}/A; A = 0.785 cm^2) of the two cells are presented in (a) and (b), respectively.

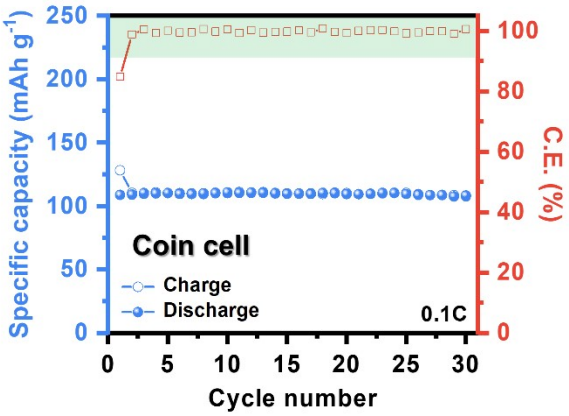

Figure S17. Cycling stability at 0.1C for a coin cell comprising the NCM composite cathode, a Celgard separator wet with the liquid electrolyte, and a Li foil anode.

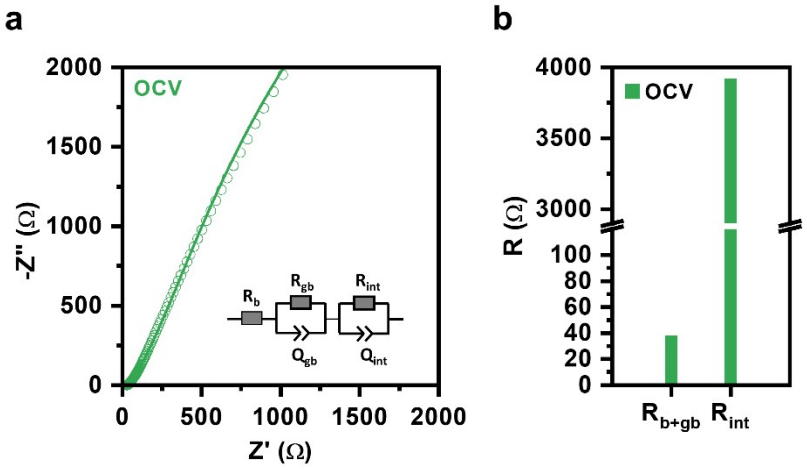

Figure S18. (a) Nyquist plot of a full cell at open circuit voltage (OCV) before cycling. Inset is an equivalent circuit used for fitting. (b) Fitted values of R_{b+gb} and R_{int} for OCV state.

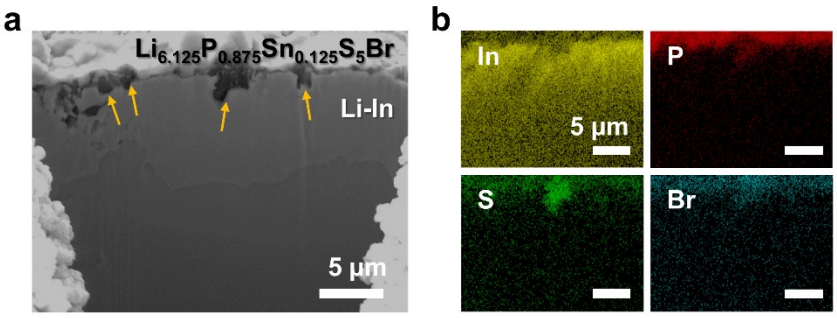

Figure S19. (a) Cross-section SEM image of the FIB-milled interface between the anode and solid electrolyte of a full cell when discharged and (b) its corresponding EDX elemental mapping (In, P, S, and Br). The orange arrows in (a) denote voids formed at the interface.

Table S1. Rietveld refinement parameters for Li_6PS_5Br (space group = F-43m, a = 9.99835(16) Å, R_{Bragg} = 2.234, GOF = 3.20). Impurities: 10.0(3) wt% Li_2S, 5.18(8) wt% LiBr.

Atom	Wyckoff Site	X	Y	Z	Occ.	B_{iso} (Å^2)
S1	4d	0.25	0.25	0.75	0.768(4)	2.408
S2	16e	0.11934(16)	-0.11934(16)	0.61934(16)	1.005(4)	1.99
S3	4a	0.0	0.0	1.0	0.232(4)	2.842
P1	4b	0.0	0.0	0.5	1.000(2)	1.579
Br1	4a	0.0	0.0	1.0	0.768(4)	2.842
Br2	4d	0.25	0.25	0.75	0.232(4)	2.408
Li1	48h	0.30710	0.02510	0.69290	0.441	4.422
Li2	24g	0.25	0.017	0.75	0.119	0.8685

Table S2. Rietveld refinement parameters for $Li_{6.075}P_{0.925}Sn_{0.075}S_5Br$ (space group = F-43m, a = 10.02087(13) Å, R_{Bragg} = 2.589, GOF = 2.00). Impurities: 2.03(13) wt% Li_2S, 1.26(5) wt% LiBr, 5.74(10) wt% $LiBr \cdot H_2O$.

Atom	Wyckoff Site	X	Y	Z	Occ.	B_{iso} (Å^2)
S1	4d	0.25	0.25	0.75	0.822(4)	2.408
S2	16e	0.12076(17)	-0.12076(17)	0.62076(17)	1.000(4)	1.99
S3	4a	0.0	0.0	1.0	0.178(4)	2.842
P1	4b	0.0	0.0	0.5	0.942(3)	1.579
Sn1	4b	0.0	0.0	0.5	0.058(3)	1.579
Br1	4a	0.0	0.0	1.0	0.822(4)	2.842
Br2	4d	0.25	0.25	0.75	0.178(4)	2.408
Li1	48h	0.30710	0.02510	0.69290	0.441	4.422
Li2	24g	0.25	0.017	0.75	0.119	0.8685

Table S3. Rietveld refinement parameters for $Li_{6.125}P_{0.875}Sn_{0.125}S_5Br$ (space group = F-43m, a = 10.02797(13) Å, R_{Bragg} = 2.434, GOF = 2.54). Impurities: 6.21(17) wt% Li_2S, 4.83(8) wt% LiBr, 3.14(13) wt% Li_4SnS_4.

Atom	Wyckoff Site	X	Y	Z	Occ.	B_{iso} (Å^2)
S1	4d	0.25	0.25	0.75	0.824(4)	2.408
S2	16e	0.11979(17)	-0.11979(17)	0.61979(17)	1.000(4)	1.99
S3	4a	0.0	0.0	1.0	0.176(4)	2.842
P1	4b	0.0	0.0	0.5	0.925(3)	1.579
Sn1	4b	0.0	0.0	0.5	0.075(3)	1.579
Br1	4a	0.0	0.0	1.0	0.824(4)	2.842
Br2	4d	0.25	0.25	0.75	0.176(4)	2.408
Li1	48h	0.30710	0.02510	0.69290	0.441	4.422
Li2	24g	0.25	0.017	0.75	0.119	0.8685

Table S4. Rietveld refinement parameters for Li_6PS_5I (space group = F-43m, a = 10.14656(10) Å, R_{Bragg} = 4.759, GOF = 2.53). Impurities: 7.0(8) wt% Li_2S.

Atom	Wyckoff Site	X	Y	Z	Occ.	B_{iso} (Å^2)
S1	4d	0.25	0.25	0.75	1.10(5)	1.295
S2	16e	0.1189(3)	-0.1189(3)	0.6189(3)	1.00(5)	1.532
P1	4b	0.0	0.0	0.5	0.96(4)	1.003
I1	4a	0.0	0.0	1.0	0.99(4)	2.361
Li1	48h	0.300(2)	0.013(7)	0.700(2)	0.37	3.079
Li2	24g	0.25	0.01(2)	0.75	0.26	3.948

Table S5. Rietveld refinement parameters for $Li_{6.1}P_{0.9}Sn_{0.1}S_5I$ (space group = F-43m, a = 10.2020(4) Å, R_{Bragg} = 4.788, GOF = 3.01). Impurities: 3.7(7) wt% Li_2S, 3.1(6) wt% $LiI{\cdot}H_2O$.

Atom	Wyckoff Site	X	Y	Z	Occ.	B_{iso} (Å^2)
S1	4d	0.25	0.25	0.75	1.02(9)	1.295
S2	16e	0.1205(4)	-0.1205(4)	0.6205(4)	1.00(9)	1.532
P1	4b	0.0	0.0	0.5	0.89(4)	1.003
Sn1	4b	0.0	0.0	0.5	0.11(4)	1.003
I1	4a	0.0	0.0	1.0	0.99(9)	2.361
Li1	48h	0.299(4)	0.003(13)	0.701(4)	0.37	3.079
Li2	24g	0.25	0.02(2)	0.75	0.26	3.948

Table S6. Rietveld refinement parameters for $Li_{6.2}P_{0.8}Sn_{0.2}S_5I$ (space group = F-43m, a = 10.21411(18) Å, R_{Bragg} = 2.207, GOF = 1.64). Impurities: 4.2(4) wt% Li_2S, 4.35(16) wt% LiI.

Atom	Wyckoff Site	X	Y	Z	Occ.	B_{iso} (Å^2)
S1	4d	0.25	0.25	0.75	1.05(5)	1.295
S2	16e	0.1208(2)	-0.1208(2)	0.6208(2)	1.04(5)	1.532
P1	4b	0.0	0.0	0.5	0.83(3)	1.003
Sn1	4b	0.0	0.0	0.5	0.17(3)	1.003
I1	4a	0.0	0.0	1.0	0.98(5)	2.361
Li1	48h	0.298(2)	0.014(6)	0.702(2)	0.37	3.079
Li2	24g	0.25	0.035(10)	0.75	0.26	3.948

Table S7. Electronic conductivities (σ_{el}) and electronic transference numbers (t_{el}) of two groups of halide Li argyrodites: $Li_{6+y}P_{1-y}Sn_yS_5Br$ and $Li_{6+z}P_{1-z}Sn_zS_5I$.

$Li_{6+y}P_{1-y}Sn_yS_5Br$			$Li_{6+z}P_{1-z}Sn_zS_5I$		
y	**σ_{el} (10^{-6} mS cm^{-1})**	**t_{el}**	**z**	**σ_{el} (10^{-6} mS cm^{-1})**	**t_{el}**
0	2.00	2.04 x 10^{-6}	0	2.00	2.50 x 10^{-4}
0.075	3.00	2.14 x 10^{-6}	0.1	2.00	3.64 x 10^{-5}
0.125	2.00	1.05 x 10^{-6}	0.2	2.00	1.43 x 10^{-5}
0.2	2.00	1.33 x 10^{-6}	0.3	1.00	9.09 x 10^{-6}

Table S8. Fitted values of the equivalent circuit elements for the Nyquist plots at the open circuit voltage (OCV), charged, and discharged states.

Values	**R_b (Ω)**	**R_{gb} (Ω)**	**C_{gb} (μF)**	**R_{int} (Ω)**		**C_{int} (mF)**	
OCV	29	9.0	46	3921		5.79	
Values	**R_b (Ω)**	**R_{gb} (Ω)**	**C_{gb} (μF)**	**R_{cse} (Ω)**	**C_{cse} (mF)**	**R_{ase} (Ω)**	**C_{ase} (mF)**
Charged	32.5	9.2	29	78.1	0.16	38.2	0.46
Discharged	35	10.1	10	102	0.24	801	1.11

Table S9. Summarized list of Li-argyrodite solid electrolytes fabricated *via* liquid-phase techniques.

Solid electrolyte	Method	Solvent	σ_{ion} (mS cm^{-1})	Air stable	Li comp-atible	Full cell (mAh g^{-1} @ cycle)	Ref.
$Li_{6+y}P_{1-y}Sn_yS_5Br$ (y = 0.125)	**Solvent-assisted**	**ACN**	**1.9**	**O**	**O**	**99 @ 50th**	**This work**
Li_6PS_5Cl	Solvent-assisted	THF	2.03	X	X	70 @ 100th	[1]
Li_6PS_5Cl-15P_2S_5	Solvent-assisted	Pyridine	4.3	X	O	86 @ 50th	[2]
Li_6PS_5Cl	Solvent-assisted	THF	1.9	X	X	132 @ 1st	[3]
Li_6PS_5Cl	Solvent-assisted	EtOH	0.21	X	O	62 @ 1st	[4]
$Li_{5.5}PS_{4.5}Cl_{1.5}$	Solvent-assisted	EDA[1)]	2.87	X	O	110 @ 10th	[5]
Li_6PS_5Cl	Solvent-assisted	EA[2)]	1.1	X	X	62 @ 25th	[6]
Li_6PS_5Cl	Co-solvent-assisted	THF/EtOH	2.4	X	X	239 @ 1st	[7]
Li_6PS_5Br	Co-solvent-assisted	THF/EtOH	3.1	X	X	110 @ 30th	[8]
Li_6PS_5Br	Co-solvent-assisted	EP/EtOH[3)]	0.034	X	X	87 @ 10th	[9]
Li_6PS_5Cl·LiCl	Co-solvent-assisted	THF/EtOH	0.53	X	O	135 @ 50th	[10]
$Li_{6.5}P_{0.5}Ge_{0.5}S_5I$	Diss.-prec.[4)]	EtOH	0.54	X	X	135 @ 100th	[11]
Li_6PS_5Br	Diss.-prec.	EtOH	0.19	X	X	55 @ 10th	[12]
Li_6PS_5Cl	Diss.-prec.	EtOH	1	X	X	90 @ 100th	[13]
Li_6PS_5Cl	Diss.-prec.	ACN/EtOH	0.6	X	X	120 @ 25th	[14]
Li_6PS_5Cl	Diss.-prec.	EtOH	0.014	X	X	45 @ 10th	[15]

1) EDA: ethylenediamine; 2) EA: ethyl acetate; 3) EP: ethyl propionate; 4) Diss.-prec.: Dissolution-precipitation

Supplementary Note S1

In principle, the sound velocity (υ_s) in a solid is proportional to the Debye frequency (ν_D), which is known to decrease with decreasing lattice vibration,[16,17] as expressed by the equation below:

$$\nu_D = \left(\frac{3N}{4\pi}\right)^{1/3} \upsilon_S$$

where N denotes the number density of atoms in a solid. Therefore, for simplicity, we will only discuss the effects of lattice vibration on the ionic conductivity afterwards.

The conventional hopping theory generally describes σ_0 of the ionic conductivity using the equation below:[16]

$$\sigma_0 = \frac{fn(Ze)^2}{k_B} e^{\Delta S_m/k_B} a_0^{\,2} \nu_0$$

where f denotes the correlation factor, n the charge carrier density, Ze the charge of the carrier, ΔS_m the entropy of the migration, a_0 the jump distance, and ν_0 the jump attempt frequency. Importantly, σ_0 is proportional to the exponential of $\Delta S_m/k_B$ multiplied by ν_0. As ΔS_m is dominated by lattice (phonon) vibration and ν_0 is generally approximated by the Debye frequency (ν_D),[16] σ_0 becomes smaller as lattice vibration decreases.

On the other hand, lattice vibration has been experimentally found to affect the activation energy (E_a) as well.[16] When there is site disorder between X^- and S^{2-} ions in Li argyrodites, E_a decreases with decreasing lattice vibration, which in turn leads to the larger $\exp(-E_a/k_BT)$.

Given the fact that the ionic conductivity is the product of σ_0 and $\exp(-E_a/k_BT)$, the ionic conductivity is barely influenced by the change in lattice vibration because of the contradicting effects of σ_0 and $\exp(-E_a/k_BT)$ on the ionic conductivity. This behavior is typically described using the Meyer-Neldel (compensation) rule.[18] One exception to this behavior is iodide argyrodites. Due to the lack of site disorder in these materials, the decrease in lattice vibration decreases σ_0 while increasing E_a (i.e., decreasing $\exp(-E_a/k_BT)$).[16]. This is the reason why iodide argyrodites have the significantly lower ionic conductivities than chloride or bromide argyrodites."

References

1. Y. J. Heo, S.-D. Seo, S.-H. Hwang, S. H. Choi and D.-W. Kim, *Int. J. Energy Res.*, 2022, **46**, 17644-17653.
2. R. Rajagopal, Y. Subramanian, Y. J. Jung, S. Kang and K.-S. Ryu, *ACS Appl. Energy Mater.*, 2022, **5**, 9266-9272.
3. M. Duchardt, M. Diels, B. Roling and S. Dehnen, *ACS Appl. Energy Mater.*, 2020, **3**, 6937-6945.
4. Z. Zhang, L. Zhang, Y. Liu, X. Yan, B. Xu and L.-m. Wang, *J. Alloys Compd.*, 2020, **812**, 152103.
5. Y. Subramanian, R. Rajagopal and K.-S. Ryu, *Scr. Mater.*, 2021, **204**, 114129.
6. S. Choi, J. Ann, J. Do, S. Lim, C. Park and D. Shin, *J. Electrochem. Soc.*, 2019, **166**, A5193.
7. L. Zhou, K.-H. Park, X. Sun, F. Lalère, T. Adermann, P. Hartmann and L. F. Nazar, *ACS Energy Lett.*, 2019, **4**, 265-270.
8. S. Yubuchi, M. Uematsu, C. Hotehama, A. Sakuda, A. Hayashi and M. Tatsumisago, *J. Mater. Chem. A*, 2019, **7**, 558-566.
9. S. Chida, A. Miura, N. C. Rosero-Navarro, M. Higuchi, N. H. H. Phuc, H. Muto, A. Matsuda and K. Tadanaga, *Ceram. Int.*, 2018, **44**, 742-746.
10. W. Arnold, D. A. Buchberger, Y. Li, M. Sunkara, T. Druffel and H. Wang, *J. Power Sources*, 2020, **464**, 228158.
11. Y. B. Song, D. H. Kim, H. Kwak, D. Han, S. Kang, J. H. Lee, S.-M. Bak, K.-W. Nam, H.-W. Lee and Y. S. Jung, *Nano Lett.*, 2020, **20**, 4337-4345.
12. S. Yubuchi, M. Uematsu, M. Deguchi, A. Hayashi and M. Tatsumisago, *ACS Appl. Energy Mater.*, 2018, **1**, 3622-3629.
13. D. H. Kim, D. Y. Oh, K. H. Park, Y. E. Choi, Y. J. Nam, H. A. Lee, S.-M. Lee and Y. S. Jung, *Nano Lett.*, 2017, **17**, 3013-3020.
14. N. C. Rosero-Navarro, A. Miura and K. Tadanaga, *J. Power Sources*, 2018, **396**, 33-40.
15. S. Yubuchi, S. Teragawa, K. Aso, K. Tadanaga, A. Hayashi and M. Tatsumisago, *J. Power Sources*, 2015, **293**, 941-945.
16. M. A. Kraft, S. P. Culver, M. Calderon, F. Böcher, T. Krauskopf, A. Senyshyn, C. Dietrich, A. Zevalkink, J. Janek and W. G. Zeier, *J. Am. Chem. Soc.*, 2017, **139**, 10909-10918.
17. O. L. Anderson, *J. Phys. Chem. Solids*, 1963, **24**, 909-917.
18. K. L. Ngai, *Solid State Ion.*, 1998, **105**, 231-235.